

Chapter 2

Passive Remote Sensing of Clouds and Precipitation

2.1 Introduction

In this dissertation, satellite measurements are used to observe the thermodynamic forcing of clouds, validate simulated cloud properties in a general circulation model (GCM), and evaluate aerosol scavenging rates. The satellite platform provides a useful vantage point for cloud studies. As will be shown in the following chapters, deep convective cloud systems span a wide spectrum of sizes, with overcast cloud decks and even precipitating structures exceeding millions of square kilometers. While ground-based and aircraft mounted observing systems provide more accurate measurements of some cloud parameters, they do not provide the necessary perspective to sample entire cloud systems on such spatial scales. Furthermore, the prohibitive cost of ship-based operations render satellites the most practical means of obtaining sufficient samples of clouds over ocean basins to perform statistical analyses of their properties.

Sampling clouds and precipitation from a satellite is by nature “remote”, meaning cloud properties must be inferred from electromagnetic radiation that reaches the satellite from a cloud that may be hundreds or thousands of kilometers below. There are generally two classes of such remote sensing, active and passive. Active remote sensing involves broadcasting radiation from an antenna and measuring the quantity and quality of the backscatter signal. An example of active remote sensing is the ground-based weather radar, which has been the workhorse of operational meteorology for decades. However, research into active remote sensing of clouds and precipitation from satellites has only recently begun.

In contrast, passive remote sensing of clouds has been done from early in the satellite age. Passive sensing is performed by measuring the natural radiation that is emitted and/or scattered by water and ice hydrometeors.

This chapter will review the physical principles underlying the passive measurements that are used extensively in this dissertation. Some elements of radiative transfer theory pertinent to all of the measurements are presented in section 2.2. Section 2.3 addresses the use of the infrared channels of the METEOSAT-5 satellite to measure cloud cover. Section 2.4 discusses the use of microwave radiation for measuring surface rain rate. Broadband measurements of terrestrial infrared radiation and reflected solar radiation are discussed in section 2.5.

2.2 Elementary radiative transfer

The radiant energy emitted by a blackbody is determined by its temperature according to the Planck function:

$$B_{\lambda} = \frac{2hc^2}{\lambda^5} \frac{1}{e^{\frac{hc}{k\lambda T}} - 1} \quad (2.1)$$

in units of watts per unit area and unit solid angle. h is the Planck constant, k is the Boltzmann constant, c is the speed of light, λ is the wavelength and T is the temperature of the blackbody. The Earth emits approximately as a blackbody at with a temperature of about 300K. The radiation transmitted to space at the top of the atmosphere, however, is a complex spectrum determined by the profile of temperature and the emission and scattering properties of gases, particulates, cloud droplets and ice crystals within the atmosphere. This spectral response allows the retrieval of many atmospheric parameters, through measurements from space, of radiances at specific frequencies. Fig. 2.1 shows the Planck curve for a blackbody radiating at 300K. As shown, terrestrial radiation peaks in the infrared region of the spectrum. In this dissertation, measurements at two frequencies in the infrared will be used to detect the presence of clouds. As will be described in section 2.3, this approach

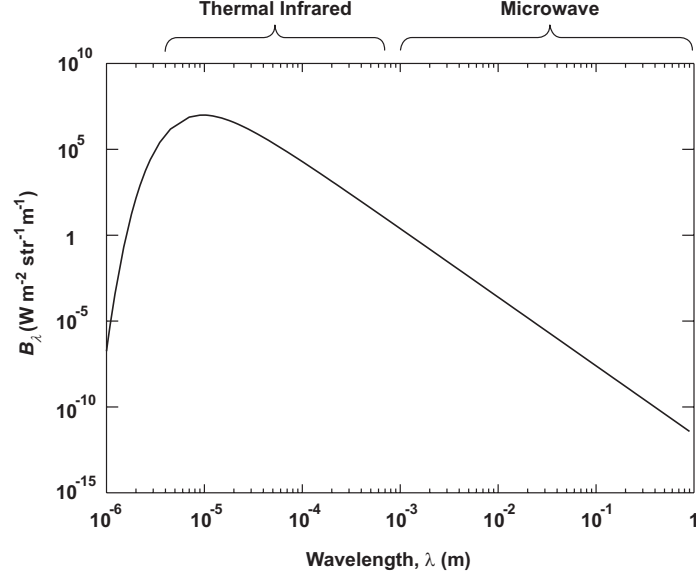


Fig 2.1. Energy emitted as a function of wavelength, given by the Planck Function, for a blackbody at 300 K.

will rely entirely on the absorption and emission by cloud drops and ice crystals, since these hydrometeors do not scatter infrared radiation. Fig. 2.1 also indicates that the long wavelength (low frequency) tail of the terrestrial emission extends into the microwave region of the spectrum. The transmission of microwaves through the atmosphere is strongly influenced by the presence of precipitation sized droplets and ice crystals. In this region of the spectrum, in addition to being subject to absorption and emission by precipitating hydrometeors, microwave radiation is also scattered by precipitating ice. This is described in more detail in section 2.4.

The fundamental equation describing the flow of radiant energy is the starting point of any satellite remote sensing study. Following Janssen (1993), the radiant intensity per unit area, unit wavelength and unit solid angle (I) along path s is given by

$$\frac{dI}{ds} = -I\alpha + S \quad (2.2)$$

where α is the extinction coefficient and S is the source term. Thus the term with α represents the loss of intensity owing to absorption and scattering in the distance ds , and

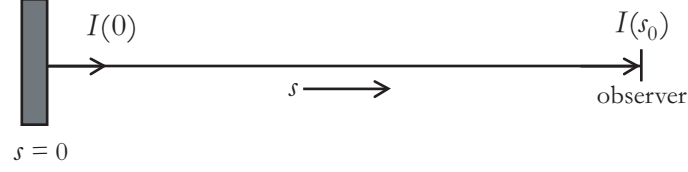


Fig 2.2. Geometry for remote sensing radiative transfer (from Janssen 1993).

the term with S represents the addition of intensity by either thermal emission or scattering of photons from other directions into the direction of ds (see diagram, Fig. 2.2). Radiant intensity is referred to interchangeably as intensity or radiance.

In the absence of scattering, losses are due only to absorption and the only source is thermal emission. In the atmosphere it is often the case that thermodynamic equilibrium prevails. This means that the energy absorbed in the section of path ds is equal to the energy emitted in ds . This is known as Kirchhoff's Law and requires that $S = \alpha B_\lambda$.

In the case without scattering, the solution to (2.1) for the intensity at location s_0 is:

$$I(s_0) = I(0)e^{-\alpha s_0} - \int_0^{s_0} B_\lambda(T(s))e^{-\alpha(s_0-s)}\alpha ds \quad (2.3)$$

Thus the intensity at s_0 includes a contribution (first term, right side of Eqn. 2.3) from the emission at the boundary $s=0$, attenuated through the entire column (in the remote sensing case, $I(s=0)$ is the intensity of the surface emission). The second term includes a contribution from each segment ds along the column, attenuated through the remaining length of the column between s and s_0 .

Equation 2.3 is sufficient to describe the cases of infrared transmission, as well as microwave transmission for wavelengths longer than about 2 cm, where contributions to α arise from absorption by cloud hydrometeors and precipitating hydrometeors respectively. However, Eqn. 2.3 is insufficient for the transmission of microwaves at wavelengths shorter than 2 cm because of contributions to α from scattering. This equation provides the intensity for a given distribution of T and α along the path s . Typically for remote sensing

applications, the problem is the inverse. Wavelengths are chosen for which the atmospheric constituent to be measured determines α . The measured value of intensity must be interpreted as an amount of the desired constituent. In many cases, there are contributions to α from several constituents so that measurements at several discrete wavelengths are required to constrain the problem.

In remote sensing studies, intensity is commonly converted to an equivalent brightness temperature, which is the temperature a blackbody would require in order to emit an intensity equal to the measured value. Thus, from Eqn. 2.1, brightness temperature can be expressed as:

$$T_B = \frac{bc}{k\lambda} \frac{1}{\ln\left(\frac{2bc^2}{I\lambda^5} + 1\right)} \quad (2.4)$$

In the discussion that follows, intensity, which is the quantity directly measured by satellite imagers, will be converted to an equivalent brightness temperature.

2.3 Infrared cloud detection

In chapter 4 of this dissertation, measurements from the METEOSAT-5 spacecraft of infrared radiation in two narrow bands are used to identify regions of overcast cloudiness. METEOSAT-5 is a geosynchronous satellite located above the equator at 63° E longitude. The spacecraft orbits at a rate of exactly once per day, so that it remains stationary relative to the nadir point on the surface of the earth below it. A diagram of the orbit characteristics appears in Fig. 2.3. The imager mounted on the spacecraft produces an image of the entire Indian Ocean basin in three narrow frequency channels every half-hour (see Fig. 1.7, p. 12 for an example of an infrared channel image). In order to generate the image, the spacecraft is oriented with its axis parallel to the longitude line below it and rotates about the axis at a rate of 2500 rotations per image (image acquisition takes 25 minutes). As the spacecraft rotates, the imager instrument scans from high southern latitudes toward high northern latitudes, completing a scan of all latitudes in about 25 minutes.

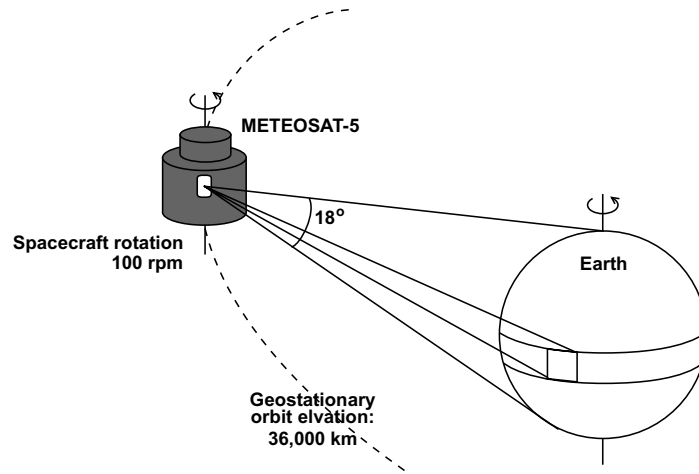


Fig 2.3. METEOSAT-5 orbit and image scanning characteristics (adapted from EUMETSAT 1999).

The cloud detection approach relies primarily on radiation at $11.5\ \mu\text{m}$ (referred to below as the IR channel). This channel is sometimes referred to as the window channel because in the $8 - 12\ \mu\text{m}$ region (also referred to as the window region) terrestrial radiation passes through the cloud-free atmosphere with almost no absorption (or top-of-atmosphere transmittance near 100% as shown in Fig. 2.4). Although the clear-sky atmosphere is nearly transparent within the window, clouds absorb strongly at these wavelengths. Even a moderately thick cloud will absorb virtually all of the upwelling terrestrial radiation passing up from below. Much of the radiance reaching the IR channel from such a cloudy column will then be the emission from the upper layer of the cloud deck. As a result, when the radiances are converted to brightness temperatures they provide an estimate of the cloud-top temperature.

Under clear-sky conditions, the IR channel measures a brightness temperature (T_{IR}) corresponding to the surface temperature (295 - 300 K for a tropical oceanic region). A brightness temperature colder than 280 K, for a 5 km METEOSAT-5 pixel, indicates that the pixel is overcast. Warmer pixels may be either clear-sky or partially filled with low, broken clouds.

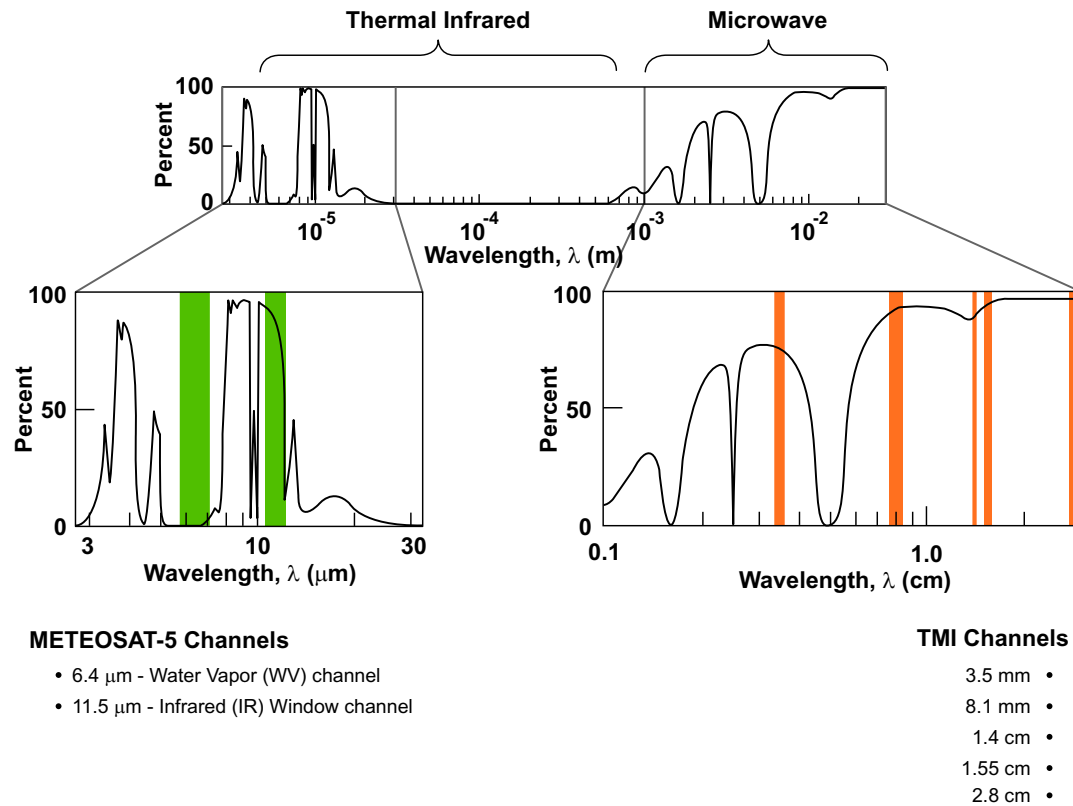


Fig 2.4. Clear-sky transmission at the top of the atmosphere for radiant energy emitted from the surface. Expanded are the spectral regions targeted by the METEOSAT-5 and TRMM Microwave Imager (TMI). Overlaid in color are the bandwidths of the imager channels. Green are METEOSAT-5 infrared channels and orange are TMI channels (adapted from Grody 1993).

There are some limitations to the use of the IR channel for cloud detection. Low clouds, such as marine stratocumulus decks, can be optically thick at the wavelength of the IR channel. However, because they are low clouds, their temperature is not very different from that of the surface. Such clouds can be difficult to distinguish from clear-sky scenes, particularly if the stratocumulus deck is broken with clear regions and cloudy regions mixed at sub-pixel spatial scales. Thin cirrus clouds can be difficult to distinguish from clear-sky scenes as well. Such clouds are often not thick enough to absorb an appreciable level of radiation in the window band.

For the case of low clouds, measurements during daylight hours of reflected solar

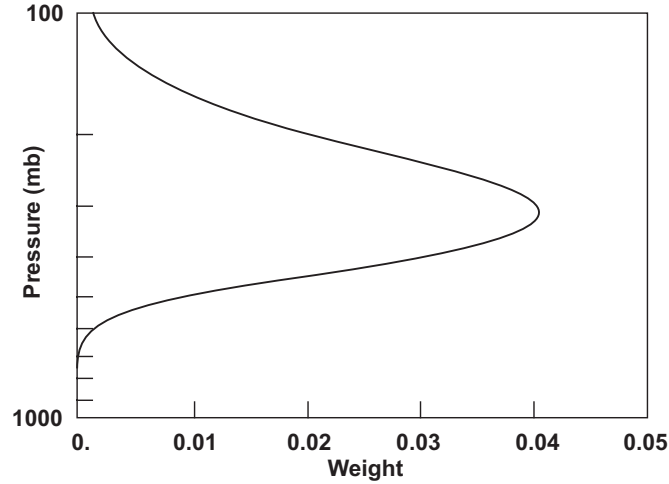


Fig 2.5. Normalized sensitivity of upwelling $6.7 \mu\text{m}$ intensity to clear-sky water vapor as a function of pressure level (from Soden and Bretherton 1993).

intensity can significantly improve their detection, as such clouds are often highly reflective.

For the purposes of this dissertation, detection of low clouds is not a priority, while tracking cloud through nighttime hours is a priority, so visible channel radiances are not used.

Thin cirrus clouds, however, are a priority in the study presented in chapter 4. A second infrared channel, centered at $6.4 \mu\text{m}$ is used for discriminating these clouds. As Fig. 2.4 indicates, virtually no surface emission within the $6.4 \mu\text{m}$ channel reaches space without being absorbed, because this channel resides on a strong water vapor absorption feature.

This channel will be referred to as the water vapor (or WV) channel. Figure 2.5 shows the relative sensitivity of the WV channel brightness temperature (T_{WV}) to changes in the water vapor amount at different altitudes, according to the radiative transfer model of Soden and Bretherton (1993). The sum of the weights over all pressure levels equals 1. T_{WV} , under cloud-free conditions, is determined by the temperature and relative humidity in a broad layer between 500 and 100 mb, corresponding to non-zero values of the sensitivity curve in Fig. 2.5. The WV channel brightness temperature decreases as relative humidity increases in the layer. Saturated conditions in the layer correspond to a brightness temperature of about 240 K for the tropical atmosphere (Roca 2000). The 500 - 100 mb layer also corresponds to the

level of middle- and upper- tropospheric clouds, which also absorb upwelling WV channel radiation. WV brightness temperatures colder than 240 K typically indicate the presence of clouds in the layer. In many instances, pixels with T_{WV} less than 240 K will also have T_{IR} less than 240 K because cloud emission is similar in the IR and WV channels. For the thin cirrus case, however, T_{IR} may be warm, indicating clear-sky conditions, because IR channel emission from the warm surface may penetrate the cloud and contribute to the T_{IR} signal in addition to the cloud emission. In this case, only the WV channel will reveal the presence of cloud because T_{WV} is insensitive to the surface emission. The thresholds ($T_{IR} < 280$ K; $T_{WV} < 240$ K) are used in chapter 4 to detect clouds. They have been validated against other multi-spectral cloud retrievals and found to be suitable for discriminating clear-sky pixels from cloudy pixels, as well as classifying mid-level and upper-level cloud types (Roca et al. 2002). Furthermore, they served as the basis for operational cloud analyses during the Indian Ocean Experiment, which successfully aided in the planning of aircraft observations during the experiment (Roca et al. 2002).

2.4 Passive microwave rain measurements

The first scanning microwave imager was flown on an experimental satellite in 1978. Since 1987, similar instruments have been present on operational meteorological satellites. Beginning with the launch of the first microwave imager, there has been a steady effort to attain reliable measurements of surface precipitation by exploiting the microwave emission and scattering properties of precipitating water and ice. In 1997, the Tropical Rainfall Measuring Mission (TRMM) satellite was launched with the specific goal of measuring the amount of tropical rainfall.

The TRMM spacecraft orbits at a much lower altitude than METEOSAT-5 and at a much faster rate (once every 90 minutes). As a result, TRMM samples the surface in diagonal swaths, approximately 760 km across (see diagram in Fig. 2.6). The standard polar orbit for meteorological satellites passes directly over the poles. The orbit rate is coordinated with the

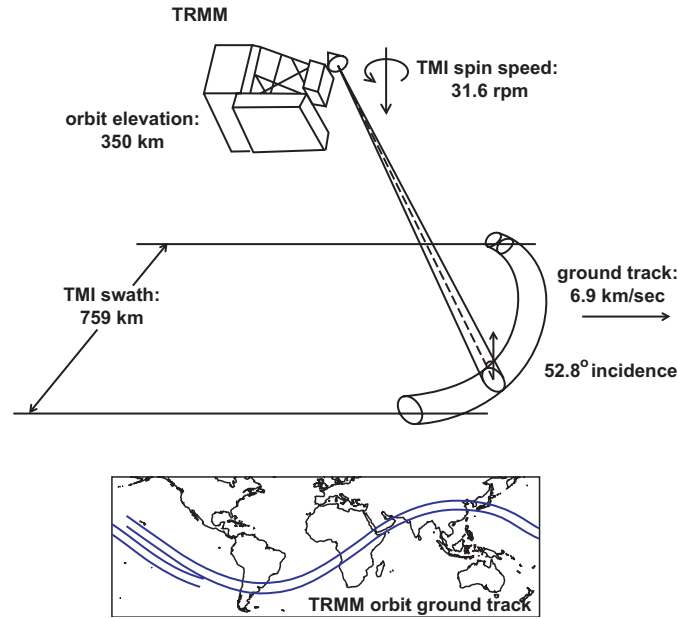


Fig 2.6. TRMM orbit and TMI scanning characteristics (adapted from Kummerow et al. 1998).

rotation of the Earth such that polar orbiting satellites cross the equator at exactly the same local time on each pass. In contrast to standard polar orbiters, the TRMM orbit is inclined at 35° latitude and is located at a lower altitude. As a result, the TRMM orbit precesses so that the local time of the equator crossing changes slightly with each orbit. This is designed to eliminate aliasing of diurnal variability in precipitation. The satellite samples all 24 local hours over the entire tropics every 45 days.

The instrument used in this dissertation is the TRMM Microwave Imager (TMI) which detects upwelling microwave radiances at 5 narrow channels within this spectral region. Additionally, 4 of these channels separately detect horizontally and vertically polarized radiation. The location of the 5 TMI wavelengths are indicated on the spectral top-of-atmosphere transmittance curve in Fig. 2.4. Within the spectral range of the TMI channels, transmittance depends on the vertically integrated tropospheric water vapor amount. Furthermore there are two distinct water vapor absorption features at approximately 5 mm and 1.35 cm. The 1.4 cm TMI channel is located on one of these features, specifically to

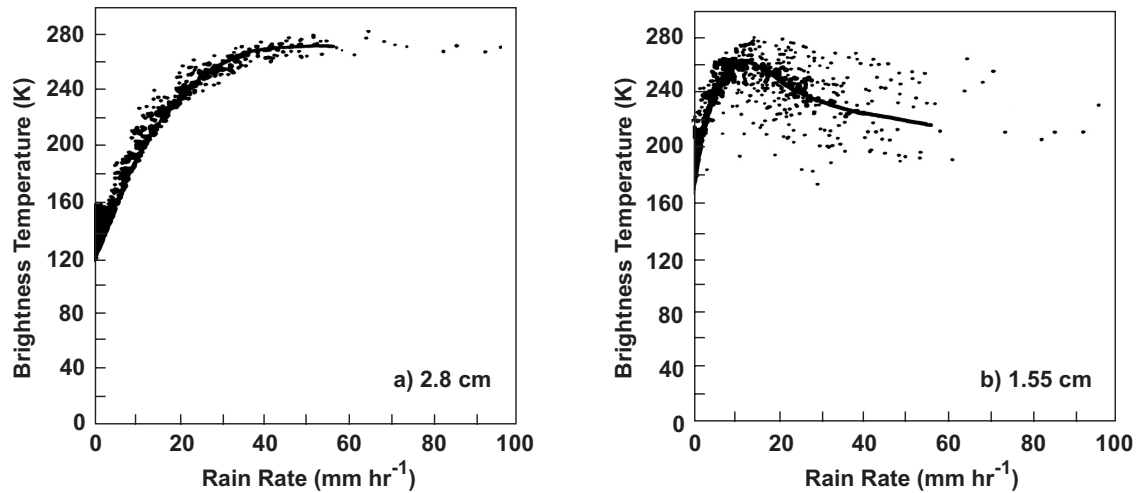


Fig 2.7. Simulated brightness temperatures as a function of rain rate for the (a) 2.8 cm and (b) 1.55 cm channels of the TMI (from Adler et al. 1991).

estimate the integrated water vapor amount and separate the water vapor effect from the precipitation effect on the brightness temperatures at the remaining channels.

Microwave precipitation detection works best over the ocean surface because emission from the ocean surface is low relative to emission from a precipitating cloud. Furthermore, the background ocean signal is spatially uniform. When viewing the ocean surface through a non-precipitating column the brightness temperature is low because the surface emissivity is low. When a precipitating cloud is present, precipitation sized water drops enhance the microwave emission of the atmosphere. As the amount of precipitating condensate increases, the microwave emission increases, and therefore the brightness temperature increases. Higher rain rates are generally correlated with thicker clouds and a greater amount of precipitating condensate, which leads to a relationship between microwave brightness temperature and surface rain rate. Fig. 2.7a shows the dependence of 2.8 cm brightness temperature on rain rate for a precipitating cloud over an ocean surface in the plane-parallel radiative transfer model of Adler et al. (1991). At the longest wavelength channels, radiation is insensitive to the presence of ice crystals in

tall clouds, therefore 2.8 cm brightness temperature increases with increasing rain rate until the signal saturates above about 40 mm hr^{-1} . At shorter wavelengths, however, significant scattering by precipitation sized ice (hail and graupel) is observed. This has the effect of reducing the measured brightness temperature, because a fraction of the upward emission from liquid raindrops will be scattered back downward by the ice above. Fig. 2.7b shows the 1.55 cm brightness temperature as a function of rain rate (Adler et al. 1991). In this simulated cloud, the rain rate is 10 mm hr^{-1} when the cloud rises to the freezing level, at which point precipitating ice begins to form. As shown in this figure, brightness temperatures at the top of the atmosphere begin to decrease as the rain rate increases above 10 mm hr^{-1} . Because the relative dependence upon emission and scattering is different for each TMI channel, each is primarily sensitive to precipitation in a different vertical level of the cloud.

For each precipitating cloud viewed by the TMI, a set of brightness temperatures is observed at 5 wavelengths. These brightness temperatures must then be inverted to a surface rain rate. This involves two steps: 1) retrieving a profile of precipitating hydrometeors from the measured brightness temperatures, and 2) relating the hydrometeor profile to a surface rain rate (usually by applying an assumed fall speed to the hydrometeor profile). The inversion problem, however, is often under-determined, meaning that the same set of brightness temperatures may correspond to several different profiles of precipitating water and ice. To help constrain the problem, it helps to know what hydrometeor profiles are likely to occur in natural clouds. For this reason, many modern approaches to the inversion problem make use of high resolution, limited area numerical models of cloud dynamics. From such models it is possible to generate candidate profiles of precipitating hydrometeors, and corresponding simulated brightness temperatures, in order to compare with observed brightness temperatures. In the data product used in this dissertation, a Bayesian approach is used to compute a linear combination of candidate profiles generated a priori from a

cloud model (Kummerow et al. 1996). Details of the inversion technique are included in section 3.2.1.

In addition to microwave rain detection, it has been demonstrated that rain rate estimates, averaged over large cloud systems, may be made using infrared brightness temperatures, such as those measured by METEOSAT-5 (Arkin and Meisner 1987). This approach relies on the correlation between the area covered by tall clouds in a region (which IR channels can measure) and the amount of rain falling in the region (which IR channels do not directly detect). IR estimates of rain rate have limited application because they rely on large spatial and/or long temporal averaging. However, for certain climate applications, they can be quite useful. This approach is used in a limited fashion in chapter 4 and a detailed discussion is presented in section 4.2.3.

2.5 Top-of-atmosphere radiative flux measurements

Top-of-atmosphere radiative flux measurements are used in chapter 3 to document the dependence of cloud radiative forcing (CRF) upon cloud and rain cell scale. These measurements are made with the Clouds and the Earth's Radiant Energy System (CERES) instrument (Wielicki et al. 1996) aboard the TRMM satellite. CERES measures upwelling radiation with three broadband radiometers. One channel measures total broadband radiance across the entire spectrum of infrared and visible wavelengths (0.2 - 100 μm). A second measures across the visible spectrum (0.2 - 5 μm), and a third one measures across the 8-12 μm infrared window. As discussed in chapter 1, CRF is calculated separately for terrestrial infrared (longwave) radiation and upwelling reflected solar (shortwave) radiation. The shortwave signal is measured directly with the CERES visible channel and the longwave signal is computed as the difference of the total channel and the visible channel.

The CERES radiometers measure radiances with an error of 1% or less. The surface footprint of each pixel is roughly 10 km and CERES scans across a swath of about 1000 km. Although the broadband fluxes reported for each pixel account for radiation

from all upwelling directions, the measurement from which the flux is derived is only a narrow radiance from a single direction. Therefore angular distribution models based on surface type and cloud cover are developed to estimate the anisotropy of the radiance. The difference between actual hemispheric fluxes and the retrieved fluxes assuming isotropy can be as large as a factor of 2. Thus the angular distribution models are the largest source of uncertainty in the retrieved fluxes. Reported errors in instantaneous top of the atmosphere fluxes for the pixel-scale data are typically 12% in the shortwave and 5% in the longwave (Suttles et al. 1992; Wielicki et al. 1995).

CRF is typically computed for time and space averages, such as monthly means over regions of hundreds of km. For this calculation, all of the CERES pixels in the region during the month are segmented into clear and cloudy. The clear pixels are then averaged to determine the mean clear-sky fluxes and all of the pixels are averaged to find the all-sky fluxes (Ramanathan et al. 1989). The difference between the clear and all-sky fluxes is the time-mean CRF (Eqns. 1.1 and 1.2). In contrast, chapter 3 will introduce measurements of instantaneous CRF for overcast pixels. This is the difference between the flux that would be observed if the cloud were not present and the flux that is actually observed. Because the clear-sky flux cannot be measured in this case, it is replaced with the monthly mean clear-sky flux. The instantaneous overcast flux is then subtracted. Variability of clear-sky fluxes over the ocean during the month adds an additional uncertainty of about 5 W m^{-2} to the measurements. For typical cloudy conditions, uncertainty in instantaneous longwave and shortwave CRF measured by CERES are about $\pm 15 \text{ W m}^{-2}$.

References

- Adler, R. F., H-Y. M. Yeh, N. Prasad, W-K. Tao, and J. Simpson, 1991: Microwave Simulations of a Tropical Rainfall System with a Three-dimensional Cloud Model. *J. Appl. Meteorol.*, **30**, 924-953.
- Arkin, P. A., and B. N. Meisner, 1987: The relationship between large-scale convective rainfall and cold cloud over the Western Hemisphere during 1982-84. *Mon. Wea. Rev.*, **115**,

51-74.

EUMETSAT, 1999: *The METEOSAT System*. 66 pp.

Grody, N. C., 1993: Remote Sensing of the Atmosphere from Satellites Using Microwave Radiometry, in *Atmospheric Remote Sensing by Microwave Radiometry* (M. A. Janssen, Ed.) John Wiley & Sons, New York, 572 pp.

Janssen, M. A., 1993: An Introduction to the Passive Microwave Remote Sensing of Atmospheres, in *Atmospheric Remote Sensing by Microwave Radiometry*, (M. A. Janssen, Ed.) John Wiley & Sons, New York, 572 pp.

Kummerow, C., W. S. Olson, and L. Giglio, 1996: A Simplified Scheme for Obtaining Precipitation and Vertical Hydrometeor Profiles from Passive Microwave Sensors. *IEEE Trans. Geosci. Remote Sensing*, **34**, 1213-1232.

Kummerow, C., W. Barnes, T. Kozu, J. Shiue, and J. Simpson, 1998: The Tropical Rainfall Measuring Mission (TRMM) Sensor Package. *J. Atmos. Ocean Technol.*, **15**, 809-817.

Ramanathan, V., R. D. Cess, E. F. Harrison, P. Minnis, B. R. Barkstrom, E. Ahmad, and D. Hartmann, 1989: Cloud-radiative forcing and climate: Results from the Earth Radiation Budget Experiment. *Science*, **243**, 57-63.

Roca, R., 2000: *Contribution à l'étude de la vapeur d'eau, de la convection et de leurs interactions dans les tropiques à l'aide d'observations de satellite et de modèles*. Ph.D. dissertation, University of Paris 7 Denis Diderot, pp. 208.

Roca, R., M. Viollier, L. Picon, and M. Desbois, 2002: A multi satellite analysis of deep convection and its moist environment over the Indian Ocean during the winter monsoon. *J. Geophys. Res.* special INDOEX issue, part 2, in press.

Soden, B. J., and F. P. Bretherton, 1993: Upper Tropospheric Relative Humidity from the GOES 6.7 mm Channel: Method and Climatology for July 1987. *J. Geophys. Res.*, **98**, 16,669-16,668.

Suttles, J. T., B. A. Wielicki, and S. Vemury, 1992: Top-of-Atmosphere Radiative Fluxes: Validation of ERBE Scanner Inversion Algorithm Using *Nimbus-7* ERB Data. *Bull. Amer. Meteor. Soc.*, **31**, 784-796.

Wielicki, B. A., R. D. Cess, M. D. King, D. A. Randall, and E. F. Harrison, 1995: Mission to Planet Earth: Role of Clouds and Radiation in Climate. *Bull. Amer. Meteor. Soc.*, **76**, 2125-2153.

Wielicki, B. A., B. R. Barkstrom, E. F. Harrison, R. B. Lee, G. L. Smith, and J. E. Cooper, 1996: Clouds and the Earth's Radiant Energy System (CERES): An Earth Observing System Experiment. *Bull. Amer. Meteor. Soc.*, **77**, 853-868.